ACS APPLIED ELECTRONIC MATERIALS

pubs.acs.org/acsaelm Article

Engineering Tunable Electronic and Photocatalytic Properties in MoSSe/AlN Heterostructures

Mohamed Farkous, Jawad El Hamdaoui,* Laura M. Pérez, Hassane Erguig, David Laroze, Aotmane En Naciri, Abdelouahad El Fatimy, and El Mustapha Feddi*

Cite This: ACS Appl. Electron. Mater. 2025, 7, 10172−10185 Read Online

ACCESS | Metrics & More | Article Recommendations | Supporting Information

ABSTRACT: We investigate MoSSe/AlN heterostructures using first-principles calculations to assess their structural stability, electronic properties, and photocatalytic potential for water splitting. Six stable stacking configurations are identified, all exhibiting indirect band gaps ranging from 0.56 to 1.20 eV (PBE) and 1.03 to 1.73 eV (HSE). Biaxial strain effectively tunes the band gap energies and can induce transitions from indirect to direct band gaps or even metallic states. Applying a perpendicular electric field further modulates the band gap, with bilayer structures showing initial band gap enlargement followed by a sharp decrease, while trilayers generally exhibit a monotonic decrease, leading to potential metallization. Unstrained AA, AB, A′A′A′, and AB′A configurations align favorably with water redox potentials, making them promising for photocatalytic water splitting. Our findings highlight the tunability of MoSSe/AlN heterostructures through stacking, strain, and electric fields, offering insights for designing advanced materials in nanoelectronics and renewable energy applications.

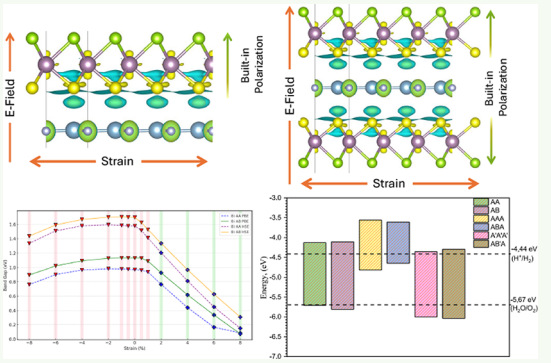

KEYWORDS: *MoSSe/AlN heterostructures, photocatalytic water splitting, band gap tuning, biaxial strain, electric field modulation*

1. INTRODUCTION

The discovery and development of two-dimensional (2D) materials have significantly advanced condensed matter physics and materials science, unveiling new phenomena and enabling innovative applications in nanoelectronics, optoelectronics, and energy storage devices.[1−4] Following the groundbreaking isolation of graphene,[5] a diverse array of layered materials, including transition metal dichalcogenides (TMDs), has attracted considerable interest due to their unique and tunable properties.[6] Among these, Janus monolayer materials such as MoSSe have emerged as intriguing candidates owing to their intrinsic structural asymmetry, where different chalcogen atoms occupy opposite sides of the molybdenum plane.[7] The broken mirror symmetry generates a built-in out-of-plane dipole that polarizes the electronic states across the heterostructure and reduces electron−hole overlap, thereby assisting charge separation. This asymmetry induces a built-in out-of-plane dipole moment, leading to novel physical phenomena and enhanced sensitivity to external stimuli such as strain and electric fields.[8,9]

The polar nature of Janus MoSSe imparts exceptional versatility in device applications. The inherent asymmetry introduces significant dipole interactions that can be manipulated via external electric fields, making MoSSe a promising candidate for field-effect transistors (FETs), photodetectors, and flexible electronics.[8−11] Integrating MoSSe with aluminum nitride (AlN) a wide-bandgap semiconductor renowned for its high thermal conductivity and piezoelectric properties[12−14] can lead to heterostructures with enhanced and tunable electronic characteristics. The synergy between the polar MoSSe and dielectric AlN facilitates effective band gap engineering, a crucial factor in developing next-generation nanoscale devices.[15]

Strain engineering and the application of external electric fields are powerful techniques for tuning the electronic properties of 2D materials.[16−18] In heterostructures like MoSSe/AlN, applying mechanical strain can significantly alter the band structure, potentially changing the material from semiconducting to metallic.[19,20] Similarly, external electric fields interact with the intrinsic dipole moments of Janus materials, inducing shifts in the conduction and valence bands.[7] These effects are particularly pronounced in MoSSe due to its polar nature, enabling precise control over its electronic behavior for applications in flexible electronics, energy-efficient devices, and photocatalysis.[9,21] Building upon these tunable electronic properties, MoSSe and its heterostructures have shown significant potential in photocatalytic

Received: August 1, 2025
Revised: November 2, 2025
Accepted: November 3, 2025
Published: November 10, 2025

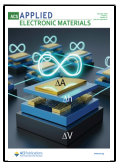

applications, particularly for water splitting, which is vital for hydrogen production and sustainable energy solutions.

The quest for sustainable energy solutions has intensified research into photocatalytic water splitting, a promising method for hydrogen production using solar energy. Photocatalysis relies on semiconductors to absorb light and generate electron−hole pairs, driving the redox reactions that split water molecules into hydrogen and oxygen.[22] The efficiency of this process is highly dependent on the photocatalyst's electronic and optical properties, particularly its band gap and the alignment of its band edges with the redox potentials of water.[23]

Forming van der Waals heterostructures by integrating 2D materials like MoSSe with other semiconductors, such as GaN and AlN, can further enhance photocatalytic performance.[24] The combination allows for optimized band alignments and improved charge transfer efficiency, essential for efficient photocatalytic reactions.[24,25] By adjusting parameters like strain and electric fields, the band structure of these heterostructures can be engineered to align the conduction and valence band edges with the redox potentials required for water splitting.[26,27] This tunability offers a versatile platform for designing high-performance photocatalysts tailored to specific energy conversion applications.

Recent studies and reviews establish Janus-MoSSe-based van der Waals heterostructures as promising photocatalysts, where the intrinsic out-of-plane polarization enables type-II alignment and efficient charge separation; notably, a MoSSe/blue-phosphorene stack reaches 19.9% predicted energy-conversion efficiency for overall water splitting.[28] Work on Janus heterostructures identifies distinctive interlayer-coupling physics and strong tunability—useful design levers for property modulation.[29,30] In parallel, theory and recent data indicate that two-dimensional III−V nitrides, including AlN and functionalized derivatives, can form stable semiconducting monolayers suitable for integration into vdW stacks[31−33] Together, these advances motivate a systematic exploration of MoSSe/AlN heterostructures and how stacking, biaxial strain, and vertical fields can be used to engineer band alignment and photocatalytic performance.

Several practical routes support the realizability of MoSSe/AlN vdW stacks. Two-dimensional AlN has been directly observed as graphite-like hexagonal nanosheets grown by plasma-MBE on Ag(111), confirming a stable 2D AlN phase.[34] Beyond noble-metal substrates, van der Waals epitaxy of AlN on monolayer TMD templates has been demonstrated at ≤ 450 °C, yielding highly oriented/crystalline AlN films on 2D layers.[35,36] Janus MoSSe itself is now routine via selective chalcogen exchange, establishing the availability of large-area Janus monolayers for stacking.[9] Related heterostructures already show the desired interfacial physics: MoSSe/g-GaN exhibits built-in fields, type-II alignment, and band edges suitable for overall water splitting, underscoring synergy between Janus TMDs and wide-gap nitrides.[37]

The stacking order in multilayer heterostructures critically influences their electronic properties by affecting interlayer coupling and charge distribution.[38] Different configurations, such as AA or AB stacking, can lead to variations in band gap values and carrier mobility due to changes in orbital overlap and van der Waals interactions.[39] Understanding these effects is essential for tailoring material properties to specific applications and forms a key aspect of our investigation into MoSSe/AlN bilayers and trilayers.[40]

Our results reveal significant tunability of the band gap across various stacking configurations and external conditions, underscoring the potential of MoSSe/AlN heterostructures for use in next-generation nanoelectronic, optoelectronic, and energy conversion devices. This work provides critical insights that could guide the design and fabrication of advanced materials with tailored properties for specific technological applications.

2. COMPUTATIONAL METHODS

All calculations were performed using the Quantum ESPRESSO package.[41] The exchange-correlation potentials were described using the generalized gradient approximation (GGA) within the Perdew−Burke−Ernzerhof (PBE) functional,[42] where the exchange-correlation energy is given by

$$E_{xc}[\rho] = \int \rho(\mathbf{r})\epsilon_{xc}[\rho(\mathbf{r})]d\mathbf{r} \tag{1}$$

where $\rho(\mathbf{r})$ is the electron density, and $\epsilon_{xc}[\rho(\mathbf{r})]$ is the exchange-correlation energy per particle.

Valence electrons were treated using normconserving pseudopotentials.[43,44] Prior to the main calculations, convergence tests were conducted on both the plane-wave cutoff energy and the k-point mesh to ensure computational accuracy.

A kinetic energy cutoff of 90 Ry was employed for the plane-wave basis set, ensuring convergence of the total energy E_{total}, calculated as

$$E_{total} = \sum_{i}^{occ} \langle \psi_i | -\frac{\hbar^2}{2m}\nabla^2 | \psi_i \rangle + E_{ext} + E_H[\rho] + E_{xc}[\rho] + E_{ion} \tag{2}$$

where ψ_i are the Kohn−Sham orbitals, E_{ext} is the external potential energy, $E_H[\rho]$ is the Hartree energy, $E_{xc}[\rho]$ is the exchange-correlation energy, and E_{ion} represents the ion−ion interaction energy.

Integration over the Brillouin zone was carried out using an 18 × 18 × 1 Monkhorst−Pack k-point mesh.[45] Geometry optimizations were performed using the Broyden-Fletcher-Goldfarb-Shanno (BFGS) algorithm. Atomic positions were relaxed until the forces on each atom were satisfied, and the total energy change between successive iterations was below 1×10^{-5} eV.

To minimize artificial interactions between periodic images, a vacuum region of 25 Å was added along the c direction perpendicular to the plane of the layers.

van der Waals (vdW) interactions were accounted for using Grimme's DFT-D3 method,[46] where the dispersion correction energy is given by

$$E_{disp} = -\sum_{i<j}\left(\frac{C_6^{ij}}{R_{ij}^6} + \frac{C_8^{ij}}{R_{ij}^8} + \frac{C_{10}^{ij}}{R_{ij}^{10}}\right) f_{damp}(R_{ij}) \tag{3}$$

with C_n^{ij} being the dispersion coefficients, R_{ij} the interatomic distances, and $f_{damp}(R_{ij})$ the damping function.

For enhanced accuracy in electronic structure calculations, the hybrid functional Heyd-Scuseria-Ernzerhof (HSE06) was employed,[47] which introduces a fraction of exact Hartree−Fock exchange into the exchange-correlation functional:

$$E_{xc}^{HSE06} = \alpha E_x^{HF,SR}(\omega) + (1-\alpha)E_x^{PBE,SR}(\omega) + E_x^{PBE,LR}(\omega) + E_c^{PBE} \tag{4}$$

where α is the mixing parameter (typically α = 0.25), ω is the screening parameter set to the default Quantum ESPRESSO value of 0.106 bohr^{-1}, $E_x^{HF,SR}$ is the short-range Hartree−Fock exchange energy, $E_x^{PBE,SR}$ and $E_x^{PBE,LR}$ are the short-range and long-range PBE exchange energies, respectively, and E_c^{PBE} is the PBE correlation energy.

https://doi.org/10.1021/acsaelm.5c01588
ACS Appl. Electron. Mater. 2025, 7, 10172−10185

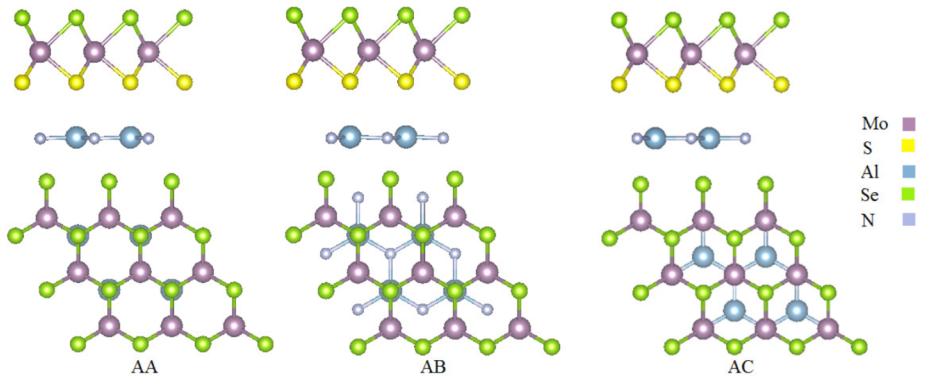

Figure 1. Atomic Structures of MoSSe/AlN Heterostructures with Varying Stacking Possibilities: AA, AB, and AC.

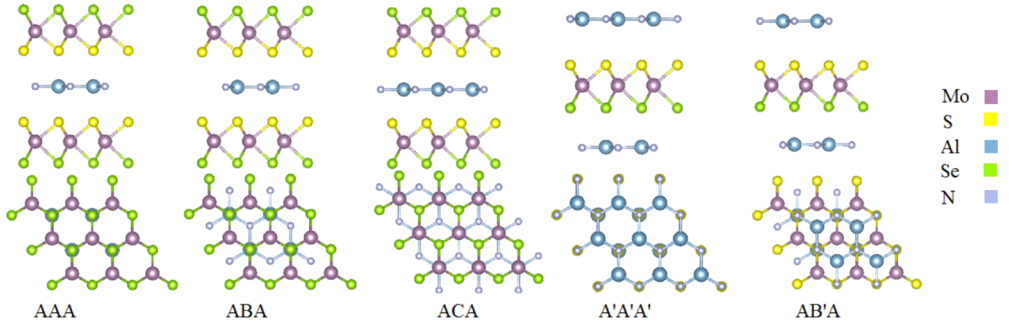

Figure 2. Atomic Configurations of MoSSe/AlN/MoSSe and AlN/MoSSe/AlN Trilayer Heterostructures with Varying Stacking Possibilities: AAA, ABA, ACA, A′A′A′, and AB′A.

The effects of an external electric field perpendicular to the layers were simulated by applying a sawtooth potential along the c axis,[48] defined as

$$V(z) = E_{\text{ext}}\left(z - \frac{L}{2}\right) \tag{5}$$

for $0 \leq z \leq L$, where E_{ext} is the magnitude of the external electric field, L is the length of the simulation cell in the c direction, and z is the coordinate along the c axis.

Phonons were computed using the finite displacement method with Phonopy[49,50] with a supercell of 4 × 4 × 1. In order to ensure the convergence of the density of states (DOS) have adopted to use a Monkhorst−Pack mesh of 18 × 18 × 1.

The relaxed monolayer lattice parameters are a_{AlN} = 3.132 Å and a_{MoSSe} = 3.220 Å. We construct the MoSSe/AlN heterostructure using a hexagonal 1 × 1/1 × 1 cell, with a lattice mismatch of about 2.7% between MoSSe and AlN. All atomic coordinates and the interlayer spacing are optimized with in-plane freedom only, while the lattice is fixed along the z axis, resulting in slightly different optimized lattice parameters for each stacking configuration. It is worth noting that, a mismatch of ∼ 2.5% is relatively small and can be accommodated either through minor in-plane strain or by forming a moiré superlattice, without introducing dislocations, as commonly observed in other 2D/III−N heterostructures.[51]

To analyze the effects of biaxial strain quantitatively, we define the biaxial strain ϵ_b in terms of the lattice constants of the monolayer before and after the strain, denoted as l_0 and l, respectively. The strain ϵ_b is then calculated as $\epsilon_b = (l - l_0)/l_0$. Here, negative and positive values represent compressive and tensile strains on the monolayer, respectively.

We calculate the elastic moduli (in kBar) and converted to two-dimensional (2D) units by multiplying with the simulation cell height along c:

$$C_{ij}^{\text{2D}}\ [\text{N/m}] = 0.01\ L_z\ [\text{Å}]\ C_{ij}^{\text{3D}}\ [\text{kBar}]$$

so that C_{ij}^{2D} denotes an areal stiffness appropriate for quasi-2D systems. Assuming an approximately hexagonal (in-plane isotropic) response, we use

$$\nu = \frac{C_{12}^{\text{2D}}}{C_{11}^{\text{2D}}}, \qquad Y^{\text{2D}} = \frac{(C_{11}^{\text{2D}})^2 - (C_{12}^{\text{2D}})^2}{C_{11}^{\text{2D}}} = (1 - \nu^2)\ C_{11}^{\text{2D}}$$

and

$$C_{66}^{\text{2D}} = \frac{C_{11}^{\text{2D}} - C_{12}^{\text{2D}}}{2}$$

It is important to emphasize that only strains feasible in experimental setups are considered. Strain engineering has been applied experimentally to graphene across different configurations.[52−54] Various methods can induce in-plane strain in mono- and multilayer structures[52,53] such as attaching them to flexible substrates, applying external loads, or using pseudomorphic growth and nanoindentation techniques for mono/bilayer systems. Experimental results have shown that monolayer graphene can sustain a maximum biaxial tensile strain up to 25%[52] before the C−C bonds break in the sheet. Additionally, in-plane strains between 6 and 11% have been reported for ultrathin MoS_2 layers[54] using nanoindentation.

3. RESULTS AND DISCUSSION

3.1. Structural Properties. In this study, we systematically explored all possible stacking configurations of MoSSe/AlN bilayer and trilayer heterostructures to assess their structural stability. For the bilayer system, a total of 12 unique stacking patterns were considered, including configurations such as AA, AB, and AC. For the trilayer system, 36 possible stacking configurations were examined, accounting for different lateral shifts and layer arrangements, including AAA, ABA, ACA, A′A′A′, and AB′A. Figures 1 and 2 illustrate the optimized atomic structures of selected MoSSe/AlN bilayer and trilayer

https://doi.org/10.1021/acsaelm.5c01588
ACS Appl. Electron. Mater. 2025, 7, 10172−10185

Table 1. Structural and Electronic Properties of MoSSe/AlN Heterostructures in Different Stacking Modes

Modes	Material	Eb	E_g^{PBE}	a	d	d_{Se-Mo}	d_{S-Mo}	d_{Al-N}	$\angle_{Se-Mo-Se}$	$\angle_{S-Mo-S}$	$\angle_{Se-Mo-S}$
AA	MoSSe-AIN	−0.289	1.671	3.177	2.969	2.519	2.402	1.834	78.163	82.782	83.513
AA	MoSSe-NAI	−0.179	1.615	3.173	3.621	2.521	2.401	1.831	77.953	82.667	83.727
AA	MoSeS-AIN	−0.304	0.968	3.177	2.790	2.521	2.401	1.835	78.101	82.820	83.528
AA	MoSeS-NAI	−0.170	1.300	3.172	3.530	2.521	2.401	1.831	77.976	82.688	83.699
AB	MoSSe-AIN	−0.273	1.542	3.180	2.981	2.516	2.404	1.835	78.332	82.778	83.410
AB	MoSSe-NAI	−0.180	1.613	3.172	3.617	2.521	2.401	1.831	77.940	82.662	83.740
AB	MoSeS-AIN	−0.317	1.129	3.180	2.718	2.524	2.398	1.837	78.102	83.051	83.373
AB	MoSeS-NAI	−0.169	1.285	3.172	3.530	2.521	2.401	1.831	77.973	82.679	83.706
AC	AlN-MoSeS	−0.237	1.663	3.174	3.164	2.518	2.399	1.832	78.091	82.801	83.550
AC	AlN-MoSSe	−0.226	1.308	3.174	3.164	2.519	2.399	1.832	78.117	82.793	83.540
AC	NAl-MoSeS	−0.179	1.619	3.175	3.319	2.517	2.400	1.832	78.169	82.787	83.510
AC	NAl-MoSSe	−0.179	1.397	3.175	3.118	2.519	2.398	1.832	78.088	82.870	83.500

heterostructures with different stacking configurations. In the bilayer structures (Figure 1), three stacking arrangements are considered: AA, AB, and AC. In the AA stacking configuration, the atoms in both the MoSSe and AlN layers are perfectly aligned; each atom in the MoSSe layer is directly above a corresponding atom in the AlN layer, which creates strong vertical interactions due to optimal orbital overlap. This alignment enhances interlayer coupling and can significantly influence the electronic properties of the heterostructure. In the AB stacking configuration, the AlN layer is shifted relative to the MoSSe layer, reducing the vertical overlap between atoms. In this case, the shifted layer's atoms occupy the hollow sites of the adjacent layer, resulting in weaker interlayer interactions compared to AA stacking. In the AC stacking configuration, the positions of the AlN and MoSSe layers are inverted relative to the AB stacking. For the trilayer structures (Figure 2), five stacking configurations are examined: AAA, ABA, ACA, A′A′A′, and AB′A. In the AAA stacking configuration, all three layers are perfectly aligned in the same manner as in the AA bilayer, maintaining vertical alignment throughout the structure. This arrangement enhances interlayer interactions and may lead to stronger coupling effects and modified electronic properties, while its symmetry can also influence the optical characteristics of the heterostructure. In the ABA stacking configuration, the first and third MoSSe layers are aligned, while the middle AlN layer is shifted relative to the outer layers. This alternating stacking pattern affects charge distribution and electronic coupling, potentially resulting in anisotropic properties and influencing charge transport across the heterostructure. In the ACA stacking configuration, the middle AlN layer is shifted differently compared to ABA, leading to distinct interlayer interactions. In the A′A′A′ stacking configuration, the MoSSe layer is sandwiched between two AlN layers, and all three layers are perfectly aligned; this enhances the interactions between the MoSSe and AlN layers and can yield unique electronic characteristics compared to AAA stacking. Finally, in the AB′A stacking configuration, the first and third AlN layers are aligned, while the middle MoSSe layer is shifted. For completeness, the full set of stacking configurations—12 for the bilayer and 36 for the trilayer systemse5—is provided in the Supporting Information. These different stacking orders significantly influence the interlayer interactions, thereby affecting the heterostructures' electronic, optical, and mechanical properties. Variations in atomic alignment alter the orbital overlaps between adjacent layers, which in turn can modify the band structures and densities of states, leading to tunable electronic properties.

4. STABILITY EVALUATION

In addition to exploring all possible stacking configurations, we evaluated their stability by performing phonon calculations for every configuration. Subsequently, binding energies were computed for all configurations, enabling us to identify the most stable structure in each heterostructure. The binding energy is defined as

$$E_b = E_{total}^{hetero} - n_{MoSSe}E_{total}^{MoSSe} - n_{AlN}E_{total}^{AlN}$$

where E_{total}^{hetero} is the total energy of the heterostructure, E_{total}^{MoSSe} and E_{total}^{AlN} are the total energies of the isolated MoSSe and AlN monolayers, respectively, and n_{MoSSe} and n_{AlN} denote the numbers of MoSSe and AlN layers in the heterostructure. More negative binding energies indicate stronger interlayer interactions and, therefore, greater stability.

For the bilayer heterostructures, our phonon calculations reveal that only two variants are dynamically stable for each stacking configuration. In the AA stacking, the stable variants are MoSeS-AlN and MoSSe-NAl, while in the AB stacking the stable variants are MoSeS-AlN and MoSeS-NAl. Additionally, for AC stacking the stable variants are AlN-MoSeS and NAl-MoSeS. Binding energy calculations (see Table 1) indicate that the MoSeS-AlN-AA and MoSeS-AIN configurations are energetically more favorable than the other bilayer variants. Consequently, for the remainder of this paper we focus solely on these two bilayer stacking configurations, which we designate as AA and AB.

For the trilayer heterostructures, in which an AlN layer is sandwiched between two MoSSe layers (i.e., in the AAA, ABA, and ACA stackings), our phonon calculations reveal the following. In the AAA stacking, the dynamically stable variants are MoSeS-Al(N)-SeMoS, MoSSe-N(Al)-SeMoS, and MoSeS-Al(N)-SMoSe. Here, the notation "Al(N)" indicates that the element shown in parentheses is offset relative to the chalcogen atoms, while the other element is perfectly aligned. In the ABA stacking, the stable variants are MoSSe-Al(N)-SeMoS and MoSSe-Al(N)-SMoSe. In contrast, within the ACA stacking the only dynamically unstable variant is SeSMo-Al(N)-MoSSe. Based on binding energy data (see Table S2 in the Supporting Information), the MoSeS-Al(N)-SMoSe configuration in both the AAA and ABA stackings is the most energetically stable. Therefore, for the remainder of this work we consider only the

https://doi.org/10.1021/acsaelm.5c01588
ACS Appl. Electron. Mater. 2025, 7, 10172−10185

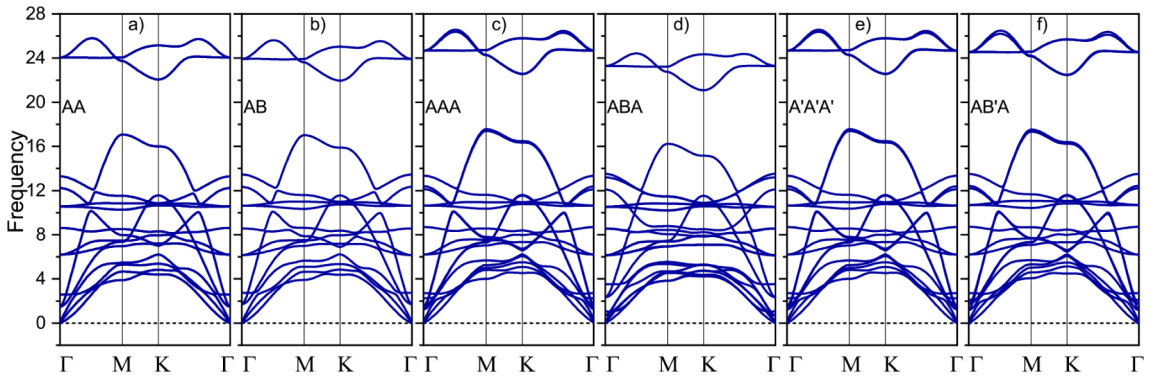

Figure 3. Phonon dispersion curves of different stacking configurations in MoSSe/AlN bilayer and trilayer heterostructures: (a) AA, (b) AB, (c) AAA, (d) ABA, (e) A′A′A′, and (f) AB′A.

MoSeS-Al(N)-SMoSe configuration in both AAA and ABA stackings. Furthermore, for the A′A′A′ and AB′A stackings, the only stable configuration identified is NAl-SMoSe-AlN, which we refer to as A′A′A′ and AB′A, respectively.

Figure 3 presents the phonon dispersion curves for the six most stable stacking configurations: AA and AB for bilayers, and AAA, ABA, A′A′A′, and AB′A for trilayers. Each plot shows the phonon frequencies as a function of the wave vector along high-symmetry paths in the Brillouin zone (Γ-M-K-Γ), with frequencies ranging from 0 to 28 THz. For clarity in our subsequent analysis, only the most stable structures are discussed in the main text; the phonon data and binding energies for the remaining configurations are provided in the Supporting Information.

4.1. In-Plane Elastic Properties and Feasibility of the Strain Window. We assessed the mechanical feasibility of the biaxial strain window by computing the in-plane elastic constants of all six dynamically stable MoSSe/AlN heterostructures. Results for the AA bilayer are shown in Figure 4, while AB, AAA, ABA, A′A′A′, and AB′A are given in the Supporting Information.

Mechanical stability was verified for every stacking and strain value using the 2D Born-like criteria:

$$C_{11}^{2D} > 0, \quad C_{66}^{2D} > 0, \quad C_{11}^{2D} > |C_{12}^{2D}|$$

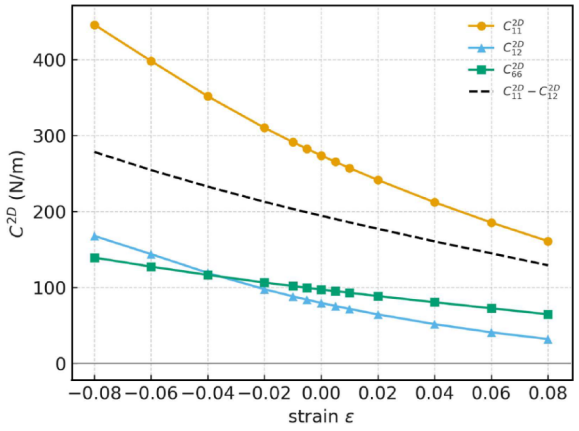

Figure 4. In-plane elastic constants of the AA bilayer as a function of biaxial strain. The dashed curve shows $C_{11}^{2D} - C_{12}^{2D}$ (with $y = 0$ reference). Positivity of $C_{11}^{2D} - C_{12}^{2D}$ and C_{66}^{2D} confirms stability.

with $C_{11}^{2D} - C_{12}^{2D}$ remaining positive for all ε (dashed curve in Figure 4). All tensors also satisfy $C_{66}^{2D} \approx \frac{1}{2}(C_{11}^{2D} - C_{12}^{2D})$, confirming internal consistency with hexagonal symmetry.

At zero strain, the effective Young's modulus Y^{2D} and Poisson's ratio ν are summarized in Table 2. Values range from

Table 2. Zero-Strain In-Plane Elastic Moduli of MoSSe/AlN Heterostructures

Stacking	Y^{2D} (N/m)	ν
AA (bilayer)	250.6	0.290
AB (bilayer)	247.5	0.287
AAA (trilayer)	371.4	0.258
ABA (trilayer)	363.8	0.255
A′A′A′ (trilayer)	359.7	0.342
AB′A (trilayer)	353.9	0.336

~ 250 N/m (bilayers) to ~ 370 N/m (trilayers), bracketed by MoS_2 (~180 N/m,[54] graphene (~340 N/m,[52] MoSSe/graphene (~459 N/m,[55] and GaN (~109 N/m,[56] confirming realistic stiffness scales.

The strain dependence of Y^{2D} is shown in Figure 5, decreasing linearly under tension and increasing under compression. Using $Y^{2D}(\varepsilon)$, the stress and elastic energy density follow

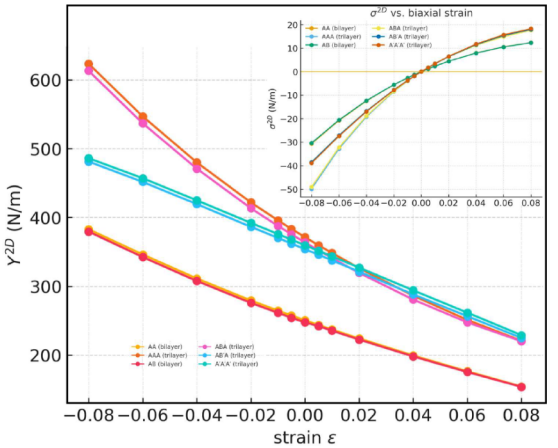

Figure 5. (Main) 2D Young's modulus Y^{2D} versus biaxial strain for all stackings. (Inset) Corresponding stress $\sigma^{2D}(\varepsilon) = Y^{2D}(\varepsilon)\varepsilon$.

https://doi.org/10.1021/acsaelm.5c01588
ACS Appl. Electron. Mater. 2025, 7, 10172−10185

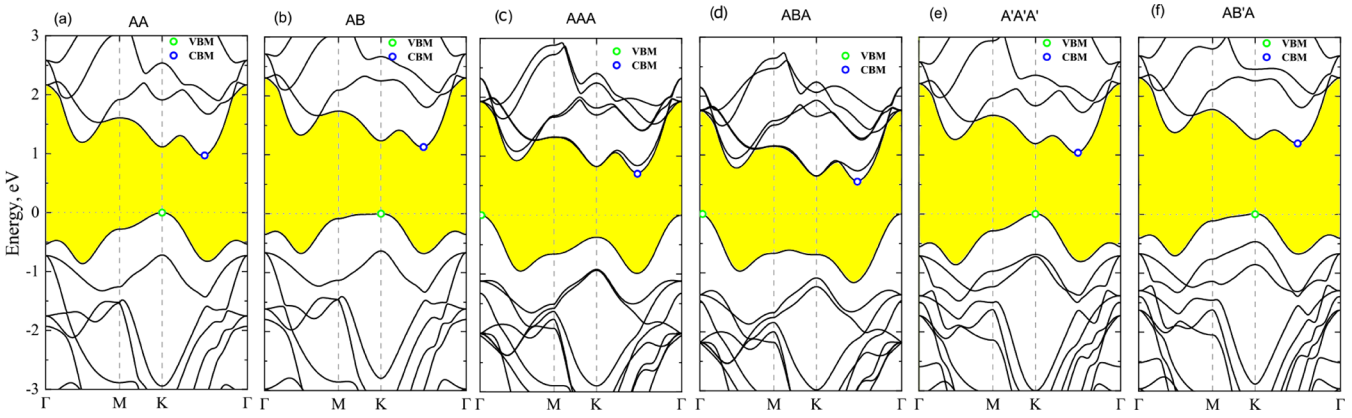

Figure 6. Band structures for stable stackings: (a) AA bilayer, (b) AB bilayer, (c) AAA trilayer, (d) ABA trilayer, (e) A′A′A′ trilayer, (f) AB′A trilayer.

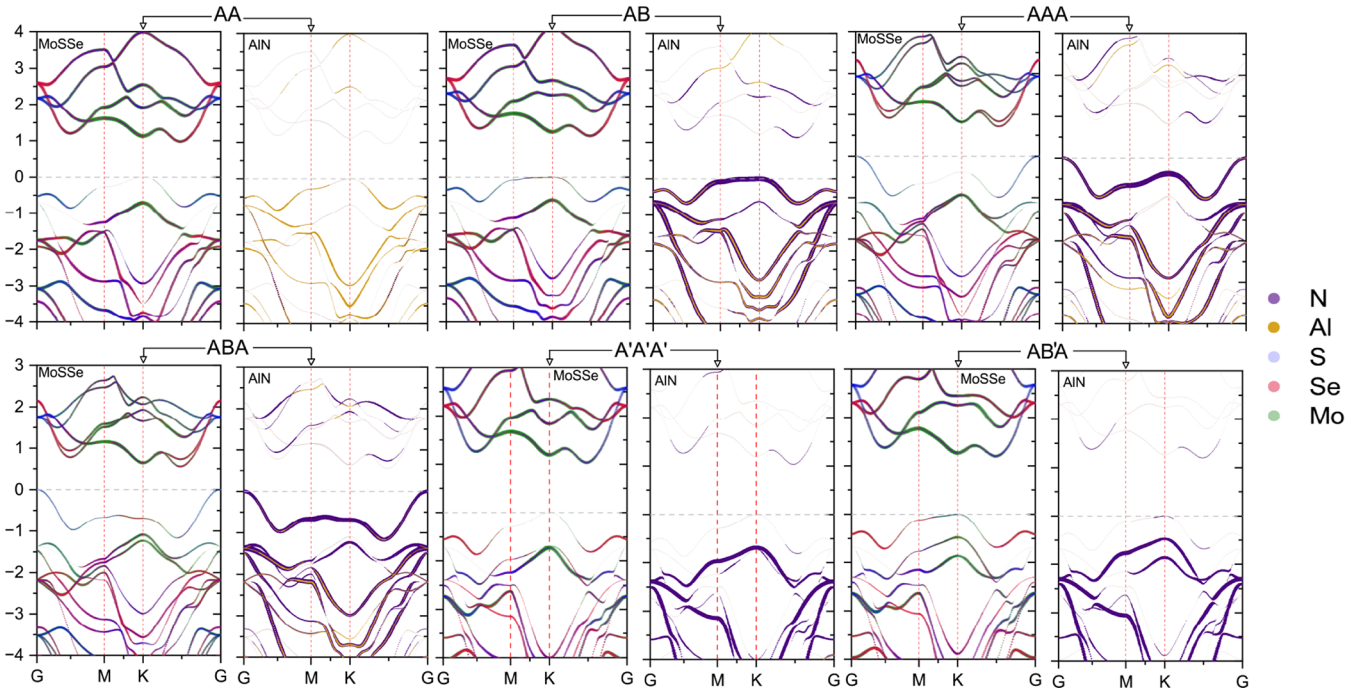

Figure 7. Projected band structures of MoSSe/AlN heterostructures for various stacking configurations.

$$\sigma^{2D}(\varepsilon) \approx Y^{2D}(\varepsilon)\varepsilon, \quad \frac{U}{A}(\varepsilon) \approx \frac{1}{2}Y^{2D}(\varepsilon)\varepsilon^2$$

At + 8% strain, stresses are 10−18 N/m depending on stacking, while at −8% they rise to 30−50 N/m, reflecting the higher cost of uniform compression. The chosen ± 8% range remains within elastic limits: for instance, the ABA trilayer (Y^{2D} ≈ 364 N/m) develops ∼ 30 N/m stress at 8% strain, well below the ∼ 150 N/m fracture strength of monolayer MoS_2.[54] Thus the applied strains are mechanically sustainable.

4.2. Electronic Properties. The electronic properties of the MoSSe/AlN heterostructures were investigated by calculating the band structures of the unstrained stable stacking configurations for both bilayer and trilayer systems, as shown in Figure 6. The yellow-shaded regions highlight the band gaps between the valence band maximum (VBM) and the conduction band minimum (CBM), marked by green and blue circles, respectively.

In the bilayer configurations, both the AA and AB stackings exhibit indirect band gaps with the VBM located at the K point and the CBM situated midway between the K and Γ points. For the AA stacking, the calculated band gap is 0.97 eV using the PBE functional, increasing to 1.58 eV with the HSE hybrid functional. The AB stacking shows slightly higher band gaps of 1.13 eV (PBE) and 1.70 eV (HSE), which can be attributed to differences in interlayer interactions due to the lateral shift between layers.

In the trilayer configurations, variations in the VBM positions are observed while maintaining indirect band gaps. The AAA and ABA stackings have the VBM at the Γ point and the CBM between the K and Γ points. The AAA stacking exhibits band gaps of 0.70 eV (PBE) and 1.25 eV (HSE), whereas the ABA stacking has slightly lower values of 0.56 eV (PBE) and 1.03 eV (HSE). The shift of the VBM to the Γ point suggests modifications in the electronic band structure due to the specific stacking sequences and interlayer interactions.

Conversely, the A′A′A′ and AB′A stackings show the VBM at the K point, with the CBM consistently located between the

https://doi.org/10.1021/acsaelm.5c01588
ACS Appl. Electron. Mater. 2025, 7, 10172−10185

K and Γ points. The A′A′A′ stacking has band gaps of 1.03 eV (PBE) and 1.65 eV (HSE), while the AB′A stacking presents the highest band gaps among the trilayer configurations, at 1.19 eV (PBE) and 1.73 eV (HSE). These differences highlight the sensitivity of the electronic properties to stacking arrangements, which influence interlayer coupling and orbital overlap.

All stable stacking configurations exhibit indirect band gaps, with the HSE functional consistently predicting larger values than PBE, addressing the common underestimation in standard DFT calculations. The ability to tune the band gap and electronic structure through stacking provides opportunities for optimizing these materials for applications in nanoelectronics and optoelectronics.

The indirect nature of the band gaps implies that optical transitions require phonon assistance, potentially affecting device efficiency. However, the tunability of the electronic properties through stacking manipulation allows for the design of materials with specific characteristics suited for devices such as photodetectors, LEDs, and photocatalysts.

To gain deeper insight into the electronic properties and interlayer interactions of the MoSSe/AlN heterostructures, we examined the projected band structures of the stable stacking configurations for both bilayer and trilayer systems as depicted in Figure 7. This analysis allows us to identify the contributions of individual layers and atomic orbitals to the valence and conduction bands, elucidating the nature of the coupling between the layers.

In the AA-stacked bilayer, the projected band structure reveals that the conduction band minimum (CBM) is predominantly contributed by the MoSSe layer, specifically through the hybridization of Mo and Se orbitals. The AlN layer exhibits a moderate contribution to the conduction band, indicating weak coupling at higher energies. Conversely, the valence band maximum (VBM) shows a strong hybridization between the AlN and MoSSe layers, with equal contributions from both. Within the AlN layer, the valence band is mainly influenced by the Al orbitals. This significant interlayer interaction at the VBM suggests enhanced coupling due to the perfect vertical alignment in the AA stacking.

For the AB-stacked bilayer, the CBM remains primarily influenced by the MoSSe layer, similar to the AA stacking, indicating weak coupling in the conduction band. However, the VBM differs by being dominated by the N orbitals of the AlN layer, with a weaker coupling between the layers compared to the AA stacking. The valence band features contributions from both layers, but the degree of overlap varies across different points in the Brillouin zone. The shift in dominance from Al to N orbitals in the AlN layer's contribution to the VBM reflects the reduced vertical overlap due to the lateral shift in the AB stacking configuration.

Comparing the two bilayer configurations, the top valence band in the AA stacking resembles that of the MoSSe monolayer, while in the AB stacking, it is more akin to the AlN monolayer. This observation highlights how stacking arrangements influence the electronic character of the heterostructure, affecting which layer's properties are more pronounced in the combined system.

In the AAA-stacked trilayer, the projected band structure indicates that the contributions from the layers are similar to those in the bilayer configurations, but with the addition of band splitting due to the increased number of layers and enhanced interlayer interactions. Notably, in the AlN layer, the splitting of bands results in two distinct bands: an upper band predominantly formed by N orbitals and a lower band primarily influenced by Al orbitals. This splitting suggests differential coupling strengths of the Al and N atoms with adjacent layers, possibly due to asymmetrical orbital overlaps or variations in interatomic distances.

The ABA stacking configuration exhibits similar features to the AAA stacking, including band splitting and layer contributions, implying that the alternating alignment of layers does not significantly alter the overall electronic interactions compared to the AAA stacking. The presence of band splitting in both configurations underscores the impact of strong interlayer coupling facilitated by the vertical alignment of layers in these stackings.

In contrast, the A′A′A′ and AB′A trilayer stackings show no band splitting in their projected band structures. In these configurations, the AlN layer's valence band is predominantly influenced by the N orbitals, indicating a shift in the primary contributing element compared to the bilayer configurations. For the MoSSe layer, there appears to be a switching of contributions between the Se and S atoms, suggesting that the stacking arrangement affects the orbital hybridization and the distribution of electronic states within the layer. The absence of band splitting suggests that the interlayer interactions are different in these configurations, possibly due to the specific arrangement of layers and the relative positions of atoms, which may lead to more symmetric interactions or reduced coupling effects.

The analysis of the projected band structures across different stacking configurations highlights the sensitivity of the electronic properties to the stacking order and interlayer interactions in the MoSSe/AlN heterostructures. In configurations with strong interlayer coupling, such as the AA and A′A′A′ stackings, there is significant hybridization of electronic states at the VBM, leading to modified electronic properties and potential applications where enhanced coupling is desirable. The band splitting observed in the trilayer configurations indicates the formation of new electronic states, which can influence carrier mobility and optical transitions.

The shifting contributions of specific atomic orbitals, such as the dominance of N orbitals in the AlN layer's valence band in certain configurations, demonstrate how stacking arrangements can be used to tailor the electronic states and influence the distribution of charge carriers. The switching of Se and S contributions in the MoSSe layer in the A′A′A′ and AB′A stackings further exemplifies the ability to modulate the electronic structure through careful design of the stacking sequence.

Upon forming the MoSSe/AlN heterostructure, the electronic density undergoes a clear redistribution that can be visualized through the charge-density difference, $\Delta\rho(\mathbf{r}) = \rho_{\mathrm{MoSSe/AlN}} - \rho_{\mathrm{MoSSe}} - \rho_{\mathrm{AlN}}$. In the AAA stacking shown in Figure 8, we observe electron accumulation vertically around Mo atoms and horizontally around S atoms, together with a strong accumulation lobe in the van der Waals gap adjacent to the MoSSe side, particularly near the S termination. Additional accumulation is visible on interfacial N atoms in the AlN layer, partially surrounded by a depletion shell. On the MoSSe side of the gap, a wavy depletion pattern appears, accompanied by significant depletion near Mo−S bonds, consistent with charge being drawn out of the Mo−S region toward the interface. These complementary accumulation/depletion features represent an interfacial polarization. Here we present the $\Delta\rho$ map

https://doi.org/10.1021/acsaelm.5c01588
ACS Appl. Electron. Mater. 2025, 7, 10172−10185

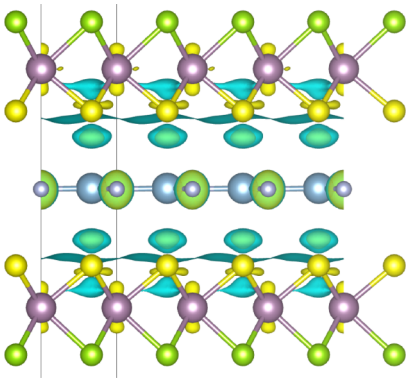

Figure 8. Charge-density difference map $\Delta\rho(\mathbf{r})$ for the AAA-stacked MoSSe/AlN heterostructure. yellow regions denote charge accumulation ($\Delta\rho > 0$) and cyan regions indicate charge depletion ($\Delta\rho < 0$). Only the AAA stacking is shown here; the corresponding maps for the remaining stable stackings are included in the Supporting Information.

for the AAA stacking as a representative example; the corresponding plots for the other stable stackings are provided in the Supporting Information.

4.2.1. Strain-Induced Band Gap Modulation. To explore the tunability of the electronic properties of MoSSe/AlN heterostructures, we investigated the impact of biaxial strain on the band gap energies of the stable bilayer and trilayer stacking configurations. Strain levels ranging from −8% (compressive) to +8% (tensile) were applied, and the resulting band structures were calculated using both the Perdew−Burke−Ernzerhof (PBE) functional and the Heyd-Scuseria-Ernzerhof (HSE) hybrid functional to ensure accurate strain-dependent behavior.

Figure 9 illustrates the band gap energies of the bilayer AA and AB stackings under various strain levels. In the AA stacking, the PBE-calculated band gap increases slightly under compressive strain, from 0.97 eV at 0% strain to 0.98 eV at −2% strain, and further to 0.76 eV at −8% strain. Under tensile strain, the band gap decreases significantly, reaching 0.94 eV at +1% strain and dropping to 0.09 eV at +8% strain. The HSE calculations reflect a similar trend, with band gaps increasing from 1.58 eV at 0% strain to 1.34 eV at −8% strain and decreasing to 0.15 eV at +8% strain.

Similarly, the AB stacking configuration shows a slight increase in band gap under compressive strain, with PBE values rising from 1.13 eV at 0% strain to 1.02 eV at −6% strain. Under tensile strain, the band gap narrows to 0.93 eV at +2% and further to 0.07 eV at +8% strain. The HSE band gaps follow the same decreasing trend, starting from 1.70 eV at 0% strain and reducing to 0.31 eV at +8% strain.

The trilayer stackings, including AAA, ABA, A′A′A′, and AB′A, exhibit similar strain-dependent behavior, as depicted in Figures 10 and 11. For the A′A′A′ and AB′A stackings, the band gaps slightly increase under compressive strain and decrease under tensile strain. Specifically, the A′A′A′ stacking's PBE band gap rises from 1.04 eV at 0% strain to 1.13 eV at −6% strain and decreases to 0.22 eV at +6% strain. The HSE-calculated band gaps follow a similar pattern, increasing to 1.41 eV under −8% strain and decreasing to 0.31 eV at +8% strain.

The AAA and ABA stackings show a more pronounced response. The AAA stacking's PBE band gap increases from 0.72 eV at 0% strain to 1.09 eV at −6% strain and decreases rapidly under tensile strain, approaching zero at strains beyond +6%. The ABA stacking exhibits a similar trend, with the band gap reducing to zero at +4% strain, indicating a transition to a metallic state under high tensile strain. To clarify the nature of this transition, we examined the total density of states (TDOS) in a ± 1.5 eV window around the Fermi level (Figure 12). The TDOS reveals that with increasing tensile strain the band gap narrows as the valence and conduction edges approach one another, until they overlap at about +4% strain. At this point, a finite DOS emerges at the Fermi level, marking the semiconductor-to-metal transition in the ABA configuration.

The band gap responses to strain in both bilayer and trilayer configurations reveal a consistent trend: compressive strain generally widens the band gap, while tensile strain narrows it. This behavior is attributed to the modulation of atomic distances and orbital overlaps under strain. Compressive strain reduces interatomic distances, enhancing orbital interactions and increasing the energy separation between the VBM and

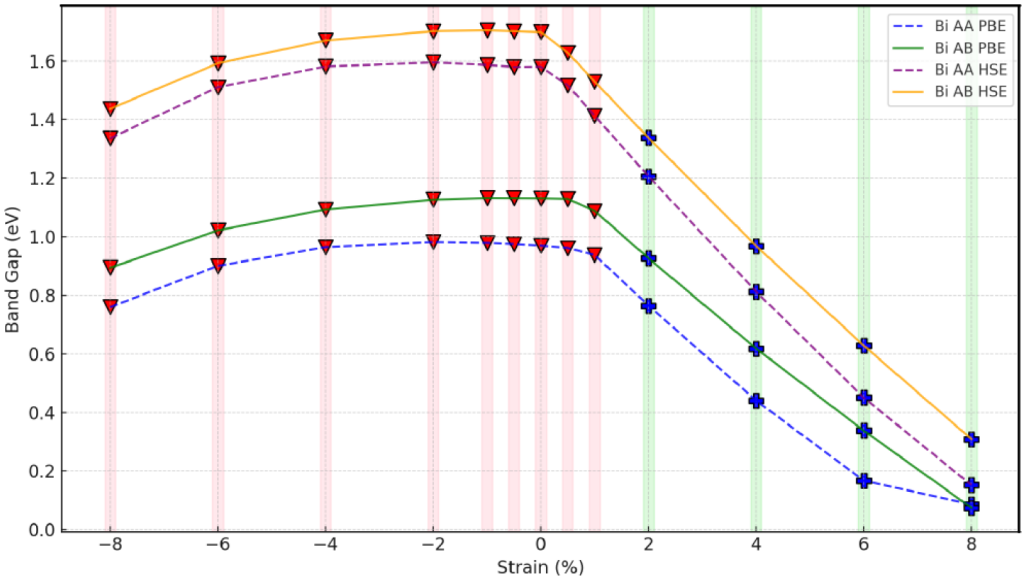

Figure 9. Effect of Strain on Band Gap in AA and AB Bilayer Heterostructures Using PBE and HSE Methods.

https://doi.org/10.1021/acsaelm.5c01588
ACS Appl. Electron. Mater. 2025, 7, 10172−10185

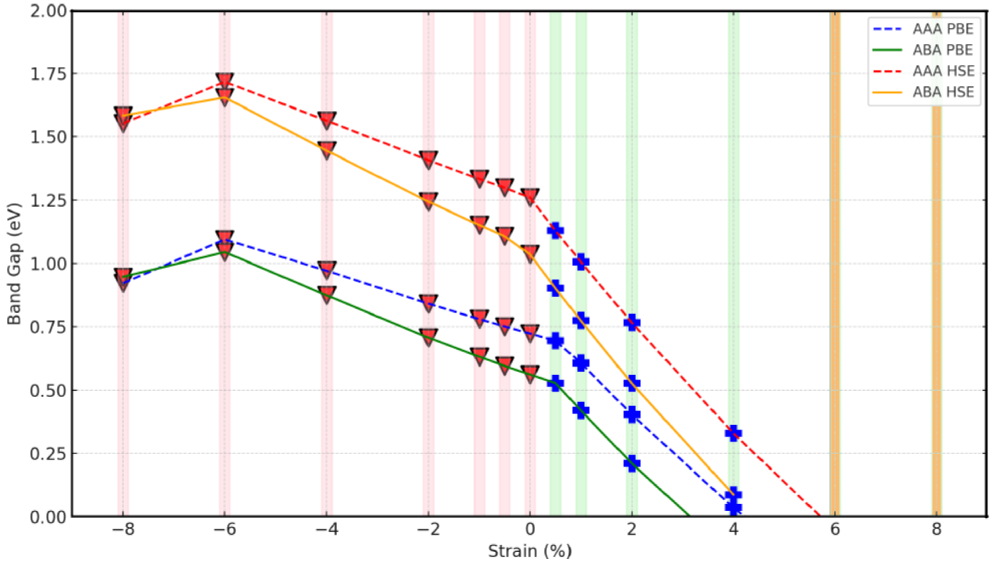

Figure 10. Effect of Strain on Band Gap in AAA and ABA Trilayer Heterostructures Using PBE and HSE Methods.

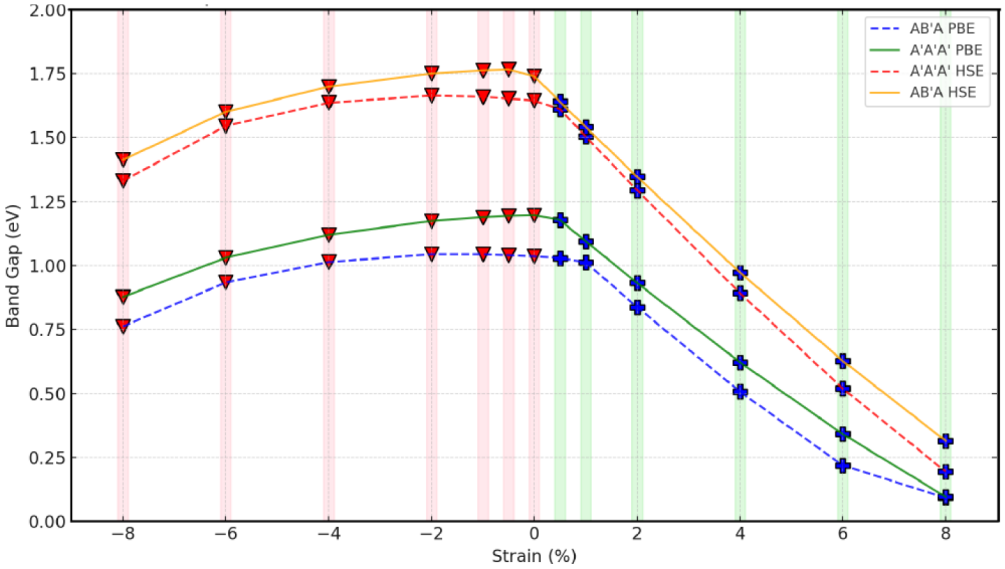

Figure 11. Effect of Strain on Band Gap in A′A′A′ and AB′A Trilayer Heterostructures Using PBE and HSE Methods.

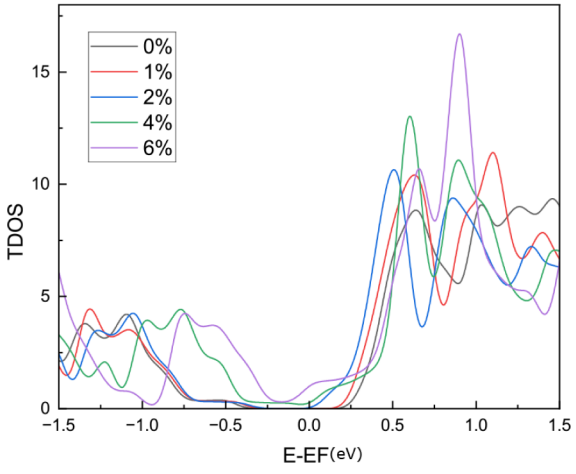

Figure 12. Total density of states (TDOS) of the ABA-stacked MoSSe/AlN heterostructure under different tensile strains.

CBM. Conversely, tensile strain elongates bonds, decreasing orbital overlap and reducing the band gap. Notably, in the ABA trilayer stacking, the band gap closes entirely under high tensile strain (+4%), indicating a possible transition to a metallic state.

Biaxial strain not only modulates the band gap energy of MoSSe/AlN heterostructures but also alters the nature of the band gap itself. Our calculations reveal that applying tensile strain induces transitions from indirect to direct band gaps and can even lead to metallic behavior in certain stacking configurations. The nature of the band gap is indicated in the Figures as red downward triangles to indicate indirect band gaps and blue crosses for direct band gaps. The background shading enhances visual clarity, with pink-tinted regions representing indirect states and green-tinted areas denoting direct regions. Metallic behavior occurs where the band gap closes under high tensile strain.

In both bilayer configurations (Bi AA and Bi AB), the unstrained structures exhibit indirect band gaps, with the valence band maximum (VBM) at the K point and the

https://doi.org/10.1021/acsaelm.5c01588
ACS Appl. Electron. Mater. 2025, 7, 10172−10185

conduction band minimum (CBM) located between the K and Γ points. As tensile strain increases beyond +1%, a transition to a direct band gap occurs, where both the VBM and CBM align at the K point. For the trilayer configurations, a similar trend is observed. The A′A′A′ and AB′A stackings maintain an indirect band gap under compressive strain and up to +0.5% tensile strain. Beyond this point, a transition to a direct band gap occurs, marked by the alignment of the VBM and CBM at the same *k*-point. This shift is significant for optoelectronic applications, as direct band gap materials are more efficient in light emission and absorption processes. In contrast, the AAA stacking remains indirect up to +2% tensile strain but becomes metallic at strains of +4% and higher. The ABA stacking also exhibits a transition to metallic behavior but at a slightly higher strain threshold, becoming metallic at +6% tensile strain.

The sensitivity of the band gap to biaxial strain in MoSSe/AlN heterostructures underscores their potential for strain-engineered electronic and optoelectronic devices. Mechanical strain can be employed to fine-tune the electronic properties to meet specific requirements, such as optimizing the band gap for photovoltaic applications or adjusting conductivity for flexible electronics. The ability to induce semiconductor-to-metal transitions through tensile strain, particularly in the ABA trilayer stacking, opens avenues for designing strain-sensitive switches and sensors. Additionally, the tunability of the band gap facilitates the customization of materials for applications like tunable lasers, photodetectors, and photocatalytic systems.

4.2.2. External Electric-Field-Induced Band Gap Modulation. The application of an external electric field is an effective method to modulate the electronic properties of van der Waals heterostructures. We investigated the influence of a perpendicular electric field on the band gap energies of the stable MoSSe/AlN bilayer and trilayer heterostructures. The electric field strength was varied from 0 to 1.5 V/Å.

Figure 13 illustrates the variation of band gap energy with the applied electric field for the bilayer AA and AB stacking

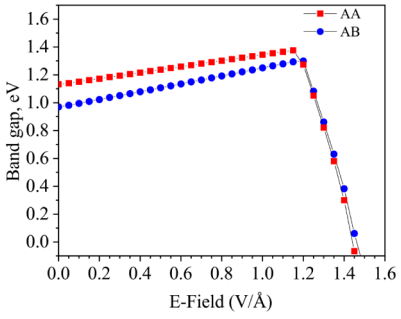

Figure 13. Effect of electric field on band gap energies in AA and AB bilayer MoSSe/AlN heterostructures.

configurations. As the electric field increases, a notable increase in the band gap energy is observed up to a certain threshold, beyond which the band gap begins to decrease sharply.

For the AA and AB stacking, the band gap energy increases gradually with the electric field, reaching a maximum of approximately 1.30 and 1.34 eV for AA and AB respectively at around 1.2 V/Å using PBE calculations. Beyond this electric field strength, the band gap decreases rapidly, indicating a possible band inversion or the onset of metallization. The consistency between the AA and AB stackings suggests that the electric field effect on the band gap is robust across different stacking arrangements in bilayer heterostructures.

The impact of the electric field on the trilayer configurations is depicted in Figures 14 and 15. In the AAA and ABA

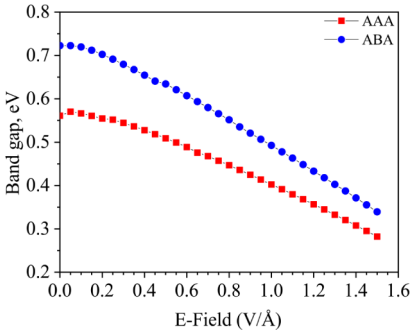

Figure 14. Effect of electric field on band gap energies in AAA and ABA trilayer MoSSe/AlN heterostructures calculated using PBE and HSE functionals.

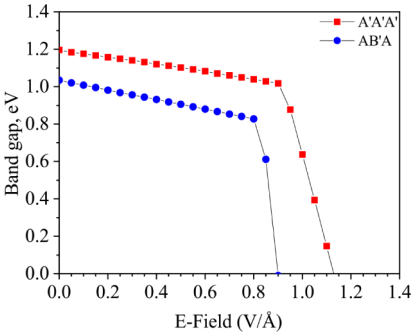

Figure 15. Effect of electric field on band gap energies in A′A′A′ and AB′A trilayer MoSSe/AlN heterostructures calculated using PBE and HSE functionals.

stackings (Figure 14), the band gap energies decrease gradually with increasing electric field. Starting from initial PBE band gaps of 0.72 eV (AAA) and 0.56 eV (ABA) at zero field, the band gaps reduce to approximately 0.34 and 0.28 eV, respectively, at an electric field strength of 1.5 V/Å. This monotonic decrease suggests that the electric field effectively narrows the band gap in these configurations, potentially enhancing electrical conductivity.

For the A′A′A′ and AB′A stackings (Figure 15), the band gap energies exhibit a more complex behavior. The A′A′A′ stacking shows a gradual decrease in band gap with increasing electric field up to around 0.85 V/Å, beyond which the band gap drops sharply, eventually closing at approximately 0.9 V/Å in PBE calculations. This indicates a transition to a metallic state induced by the electric field. The AB′A stacking also demonstrates a decrease in band gap with increasing electric field. The band gap decreases steadily and reaches zero at around 1.15 V/Å. This suggests that the AB′A and A′A′A′ stacking can undergo an electric field-induced semiconductor-to-metal transition, which could be exploited in electronic devices such as field-effect transistors and switches.

The electric field-induced modulation of the band gap in MoSSe/AlN heterostructures can be attributed to the Stark effect, where the external field alters the potential landscape experienced by the charge carriers. In bilayer configurations, the initial increase in band gap with electric field is due to the

https://doi.org/10.1021/acsaelm.5c01588
ACS Appl. Electron. Mater. 2025, 7, 10172−10185

field enhancing the separation between electron and hole states, effectively widening the band gap. Beyond a certain threshold field strength (approximately 1.2 V/Å), the field becomes strong enough to cause significant band bending or overlap, leading to a reduction in band gap and eventual closure.

In trilayer configurations, the continuous decrease in band gap with increasing electric field suggests that the field effectively reduces the energy difference between the VBM and CBM. The more complex behavior in A′A′A′ and AB′A stackings, including the abrupt band gap closure, indicates that the interlayer coupling and the asymmetry introduced by the stacking sequence play crucial roles in determining the electronic response to the electric field.

4.3. Photocatalytic Water Splitting. The photocatalytic water splitting ability of the MoSSe/AlN heterostructures was evaluated by analyzing the alignment of their electronic band edges relative to the redox potentials of water. For effective overall water splitting, the conduction band minimum (CBM) should be higher (more negative in energy) than the hydrogen evolution potential (H_2/H_2O reduction potential at − 4.44 eV), while the valence band maximum (VBM) should be lower (more positive in energy) than the oxygen evolution potential (H_2O/O_2 oxidation potential at − 5.67 eV).[23] This alignment ensures that the photogenerated electrons and holes have sufficient potential to drive the hydrogen and oxygen evolution reactions, respectively.

In their unstrained states, the bilayer configurations AA and AB, as well as the trilayer configurations A′A′A′ and AB′A, exhibit favorable band edge alignments for overall water splitting. As shown in Figure 16, the CBM of these

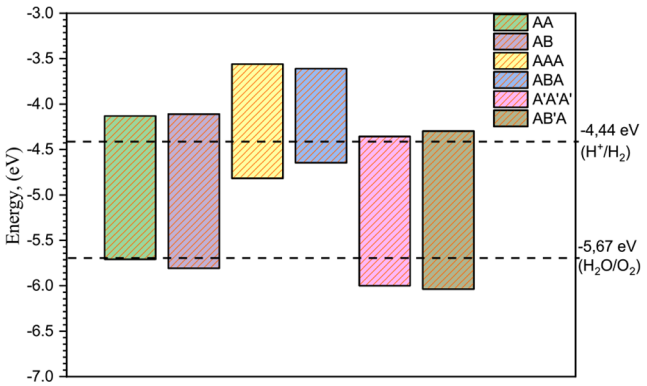

Figure 16. Band edge positions of unstrained MoSSe/AlN heterostructures relative to the vacuum level.

configurations is located above the hydrogen evolution potential, and the VBM is below the oxygen evolution potential. This positioning allows the photogenerated electrons at the CBM to reduce protons to hydrogen gas, while the holes at the VBM can oxidize water molecules to oxygen gas. Therefore, these heterostructures are promising candidates for efficient photocatalytic water-splitting applications.

In contrast, the trilayer configurations AAA and ABA are unsuitable for overall water splitting in their unstrained states. Their CBM lies below (less negative than) the hydrogen evolution potential and their VBM is above (more positive than) the oxygen evolution potential, as depicted in Figure 16. This unfavorable alignment means that the photogenerated charge carriers lack the necessary potential to drive the oxygen evolution reaction effectively.

To benchmark these results, Table 3 compares the unstrained band-edge positions (vs vacuum) and photocatalytic classification for MoSSe/AlN against related vdW stacks (MoSSe/GaN, MoS_2/AlN, and WS_2/AlN). This benchmarking underscores that MoSSe/AlN belongs to the subset of TMD/nitride heterostructures that can already drive overall water splitting without cocatalysts, motivating the following analysis of how biaxial strain further tunes these alignments. The application of biaxial strain alters the electronic band structure of the heterostructures, thereby affecting their photocatalytic capabilities. Figure 17 illustrates the effect of strain on the band edge positions of the bilayer and trilayer configurations, respectively. For the AA and AB bilayer configurations, applying tensile strain (positive strain values) causes the CBM to move closer to the hydrogen evolution potential. Under the tensile strain of approximately +6%, the CBM drops below the − 4.44 eV threshold, as shown in Figure 17. This shift renders the CBM less negative than the hydrogen evolution potential, making it ineffective for driving the hydrogen evolution reaction. Similarly, under the compressive strain of −8%, the CBM drops below the hydrogen evolution potential, leading to decreased photocatalytic efficiency for hydrogen production.

Table 3. Band-Edge Positions vs. Vacuum, Band Gaps, Strain Sensitivity, and Photocatalytic Classification of Our Materials and Some Other TMD/Nitride Heterostructures

System	E_{CBM} (eV)	E_{VBM} (eV)	E_g (eV)	Strain tunability	Photocatalytic
MoSSe/AlN	−4.13	−5.7101	1.58	High	Overall (HER +OER)
MoSSe/AlN/MoSSe	−3.5595	−4.8185	1.25	High	HER only
AlN/MoSSe/AlN	−4.3568	−6.0003	1.64	High	Overall (HER +OER)
$MoSe_2$/AlN	−3.6[57]	−5.1[57]	1.52[57]	High[57]	HER only
WS_2/AlN	−3.9[57]	−5.3[57]	1.8[57]	High[40]	HER only
MoSSe/GaN	−4.2[37]	−5.7[37]	1.5[37]	High[40]	Overall (HER +OER)

The A′A′A′ trilayer configuration exhibits favorable band edge alignment under compressive strain up to −4%. In this strain range, the CBM remains above the hydrogen evolution potential, and the VBM is below the oxygen evolution potential. This alignment indicates suitability for overall water splitting. However, as the strain becomes tensile beyond +1%, the CBM shifts below the hydrogen evolution potential, diminishing its ability to drive the hydrogen evolution reaction effectively. In contrast, the AAA and ABA trilayer configurations remain unsuitable for overall water splitting across the entire strain range studied. Their CBM stays below the hydrogen evolution potential, and the VBM is above the oxygen evolution potential, as shown in Figure 17. Although compressive strain slightly modifies the band edges, it is insufficient to achieve the necessary alignment for photocatalytic activity. The strain-dependent shifts in the band edge positions can be attributed to the alteration of atomic orbitals and bond lengths under mechanical deformation. Compressive strain generally leads to a widening of the band gap and an

https://doi.org/10.1021/acsaelm.5c01588
ACS Appl. Electron. Mater. 2025, 7, 10172−10185

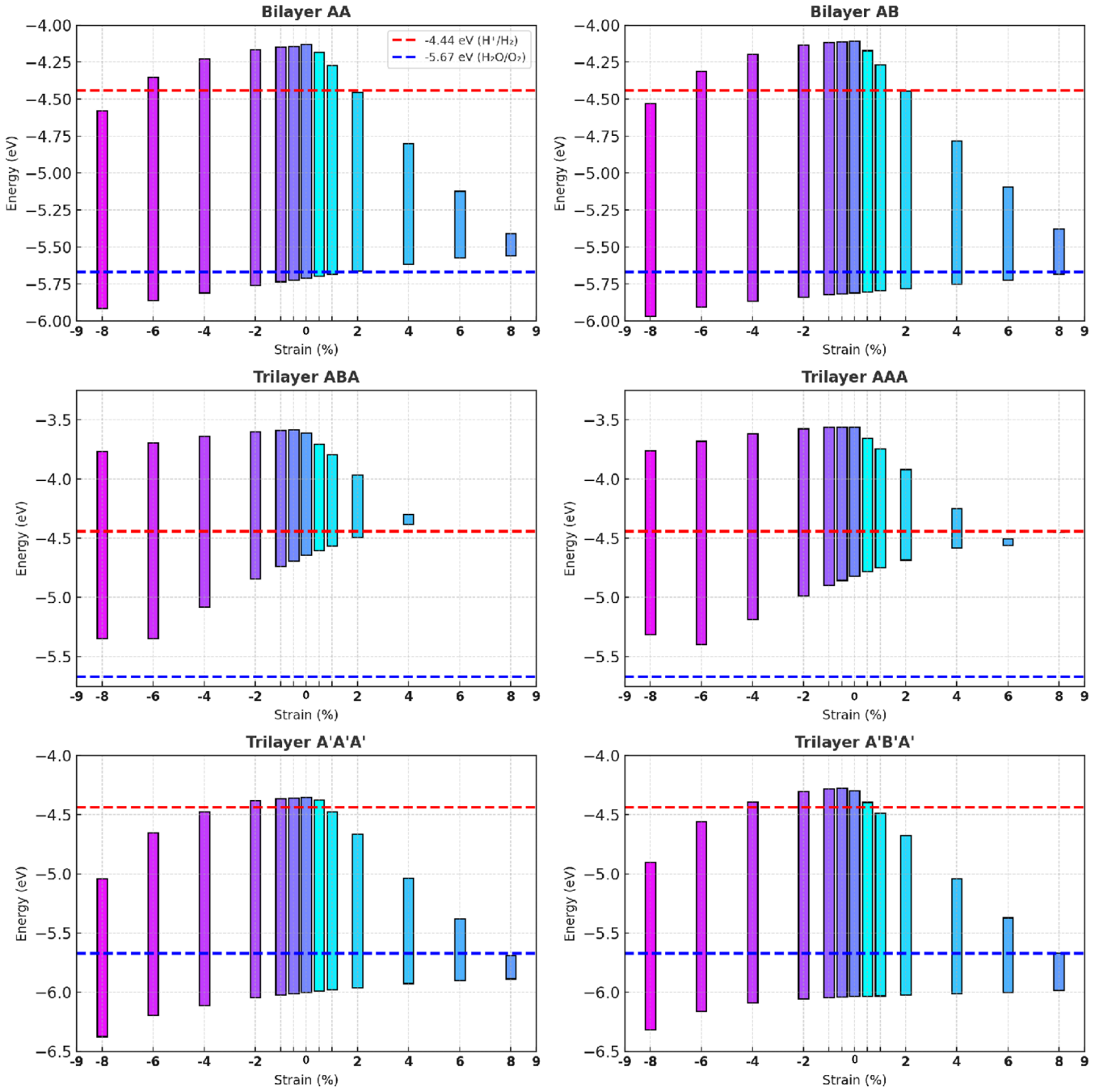

Figure 17. Effect of biaxial strain on the band edge positions of MoSSe/AlN heterostructures.

upward shift (toward more negative values) of the CBM and VBM relative to the vacuum level. This shift can enhance the photocatalytic activity if it results in better alignment with the redox potentials of water splitting.

5. CONCLUSIONS

In summary, our first-principles study reveals that MoSSe/AlN heterostructures possess tunable electronic and photocatalytic properties influenced by stacking configurations, biaxial strain, and external electric fields. Six stable structures were identified, all with indirect band gaps that can be modulated via mechanical and electrical means. Biaxial strain allows for precise control over the band gap energy and nature, enabling transitions to direct band gaps or metallic states. Electric fields further adjust the electronic properties, with potential applications in electronic switches and field-effect devices. Importantly, certain configurations exhibit suitable band edge alignments for photocatalytic water splitting, which can be enhanced through strain engineering. These insights demonstrate the versatility of MoSSe/AlN heterostructures for applications in nanoelectronics, optoelectronics, and renewable energy technologies, paving the way for future experimental and theoretical explorations to optimize their performance.

■ ASSOCIATED CONTENT

Supporting Information

The Supporting Information is available free of charge at https://pubs.acs.org/doi/10.1021/acsaelm.5c01588.

https://doi.org/10.1021/acsaelm.5c01588
ACS Appl. Electron. Mater. 2025, 7, 10172−10185

Computational details and convergence tests (plane-wave energy cutoff; Monkhorst−Pack k-point sampling); tables of total and binding energies for MoSSe/AlN bilayer and trilayer stackings (AA, AB, ABA, AB′A, A′A′A′); phonon dispersion curves with bottom/side views indicating dynamical stability; interlayer registry diagrams; in-plane elastic constants versus biaxial strain; charge density difference maps showing charge accumulation and depletion (PDF)

AUTHOR INFORMATION

Corresponding Authors

Jawad El Hamdaoui − *School of Applied and Engineering Physics, Mohammed VI Polytechnic University, Ben Guerir 43150, Morocco*; Email: jawad.elhamdaoui@um6p.ma

El Mustapha Feddi − *School of Applied and Engineering Physics, Mohammed VI Polytechnic University, Ben Guerir 43150, Morocco*; orcid.org/0009-0000-3333-8540; Email: e.feddi@um5s.net.ma

Authors

Mohamed Farkous − *Materials Physics and Subatomic Laboratory, Superior School of Technology, IBN-Tofail University, Kenitra 14000, Morocco*

Laura M. Pérez − *Departamento de Ingeniería Industrial y de Sistemas, Universidad de Tarapacá, Arica 1000000, Chile*

Hassane Erguig − *Materials Physics and Subatomic Laboratory, Superior School of Technology, IBN-Tofail University, Kenitra 14000, Morocco*

David Laroze − *Instituto de Alta Investigación, Universidad de Tarapacá, Arica 1000000, Chile*

Aotmane En Naciri − *LCP-A2MC, ICPM, Université de Lorraine, Metz 57070, France*

Abdelouahad El Fatimy − *School of Applied and Engineering Physics, Mohammed VI Polytechnic University, Ben Guerir 43150, Morocco*; orcid.org/0000-0001-6500-7762

Complete contact information is available at: https://pubs.acs.org/10.1021/acsaelm.5c01588

Author Contributions

Conceptualization: M.F.; J.E.H.; E.M.F.; A.E. F.; Methodology: M.F.; J.E.H.; Software: M.F.; Validation: J.E.H.; L.M.P.; D.L.; Formal analysis: M. F.; J.E.H.; Investigation: M.F.; J.E.H.; Data curation: M.F.; Visualization: M.F.; L.M.P.; Writing-original draft: M.F.; Writing-review and editing: M.F.; J.E.H.; L.M.P.; H.E.; D.L.; A.E.N.; A.E.F.; E. M.F.; Resources: A.E.F.; D.L.; E.M.F.; Supervision: E.M.F.; J.E.H.; Project administration: E.M.F.; A.E.F.; Funding acquisition: D.L.; L.M.P.; A.E.F.

Notes

The authors declare no competing financial interest.

ACKNOWLEDGMENTS

DL and LMP acknowledge partial financial support from FONDECYT 1240985 and Centers of Excellence with BASAL/ANID financing, Grant No. CIA250002, CEDENNA.

REFERENCES

(1) Xu, M.; Liang, T.; Shi, M.; Chen, H. Graphene-like Two-dimensional Materials. *Chem. Rev.* **2013**, *113*, 3766−3798.

(2) Lin, T.; Zeng, Y.; Liao, X.; Li, J.; Zhou, C.; Wang, W. Two-dimensional Material/Group-III Nitride Hetero-structures and Devices. *Rep. Prog. Phys.* **2025**, *88*, 046501.

(3) Liu, C.; Cui, Z.; Zhang, S.; Wang, L. High Sensitivity Photodetectors of PtS2/AlN and PtSe2/AlN Heterostructures. *J. Phys. Chem. Solids* **2024**, *194*, 112255.

(4) Li, L.; He, Y.; Lin, T.; Jiang, H.; Li, Y.; Lin, T.; Zhou, C.; Li, G.; Wang, W. MXene/AlGaN van der Waals Heterojunction Self-powered Photodetectors for Deep Ultraviolet Communication. *Appl. Phys. Lett.* **2024**, *124*, 132105.

(5) Novoselov, K.; Geim, A.; Morozov, S.; Jiang, D.; Zhang, Y.; Dubonos, S.; Grigorieva, I.; Firsov, A. Electric Field Effect in Atomically Thin Carbon Films. *Science* **2004**, *306*, 666−669.

(6) Wang, Q.; Kalantar-Zadeh, K.; Kis, A.; Coleman, J.; Strano, M. Electronics and Optoelectronics of Two-dimensional Transition Metal Dichalcogenides. *Nat. Nanotechnol.* **2012**, *7*, 699−712.

(7) Dong, L.; Lou, J.; Shenoy, V. B. Large In-plane and Vertical Piezoelectricity in Janus Transition Metal Dichalcogenides. *ACS Nano* **2017**, *11*, 8242−8248.

(8) Zhang, J.; Jia, S.; Kholmanov, I.; Dong, L.; Er, D.; Chen, W.; Guo, H.; Jin, Z.; Shenoy, V. B.; Shi, L.; et al. Janus Monolayer Transition-metal Dichalcogenides. *ACS Nano* **2017**, *11*, 8192−8198.

(9) Lu, A.; Zhu, H.; Xiao, J.; Chuu, C.; Han, Y.; Chiu, M.; Cheng, C.; Yang, C.; Wei, K.; Yang, Y.; et al. Janus Monolayers of Transition Metal Dichalcogenides. *Nat. Nanotechnol.* **2017**, *12*, 744−749.

(10) Lin, Z.; Chen, J.; Zheng, Z.; Lai, Q.; Liu, Z.; Liu, L.; Xiao, J.; Wang, W. Multifunctional UV Photodetect-Memristors Based on Area Selective Fabricated Ga2S3/Graphene/GaN van der Waals Heterojunctions. *Mater. Horiz.* **2025**, *12*, 3091−3104.

(11) Jiang, H.; Wang, H.; Wang, W.; Li, G. Two-dimensional GaN/Si Heterojunctions towards High-performance UV-B Photodetectors. *Mater. Horiz.* **2025**, *12*, 4379−4387.

(12) Ambacher, O. Growth and Applications of Group III-Nitrides. *J. Phys. D: appl. Phys.* **1998**, *31*, 2653.

(13) Yelgel, Ö. C. The Role of Intrinsic Atomic Defects in a Janus MoSSe/XN (X = Al, Ga) Heterostructure: A First Principles Study. *Condens. Matter Phys.* **2023**, *26*, 43703.

(14) Lin, T.; Wang, W. Polarization-sensitive Self-powered MoS2/a-GaN Heterojunction Photodetectors for Ultraviolet Polarized Imaging. *Appl. Phys. Lett.*, 2024, *124*, .

(15) Zengin, Y.; Caglayan, R.; Mogulkoc, Y. Adsorption of Small Gas Molecules onto the Two-dimensional Janus SnSSe Monolayer. *Comput. Condens. Matter* **2023**, *36*, No. e00815.

(16) He, K.; Poole, C.; Mak, K.; Shan, J. Experimental Demonstration of Continuous Electronic Structure Tuning via Strain in Atomically Thin MoS2. *Nano Lett.* **2013**, *13*, 2931−2936.

(17) RoldÁn, R.; Castellanos Gomez, A.; Cappelluti, E.; Guinea, F. Strain Engineering in Semiconducting Two-dimensional Crystals. *J. Phys.: condens. Matter* **2015**, *27*, 313201.

(18) Liu, Y.; Yang, Z.; Jiang, Z.; Qian, Q.; Zhou, S.; Cao, W.; Liu, H.; Qian, K.; Han, L.; Cao, R. Electronic Properties of Janus TMD WSSe/WX2 (X = S, Se) Heterostructure by External Strain: A Hybrid Functional Study. *ACS Appl. Energy Mater.* **2024**, *7*, 9986−9995.

(19) Yuan, J.; Shan, Y.; Li, T. Electronic Structure and Hydrogen Evolution Reaction in Janus Monolayer MoSSe Regulated by Strain Engineering. *J. Phys. D: appl. Phys.* **2020**, *53*, 125502.

(20) Zhang, W.; Huang, Z.; Zhang, W.; Li, Y. Two-dimensional Semiconductors with Possible High Room Temperature Mobility. *Nano Res.* **2014**, *7*, 1731−1737.

(21) Ma, X.; Wu, X.; Wang, H.; Wang, Y. A Janus MoSSe Monolayer: A Potential Wide Solar-spectrum Water-splitting Photocatalyst with a Low Carrier Recombination Rate. *J. Mater. Chem. A* **2018**, *6*, 2295−2301.

(22) Fujishima, A.; Honda, K. Electrochemical Photolysis of Water at a Semiconductor Electrode. *Nature* **1972**, *238*, 37−38.

(23) Kudo, A.; Miseki, Y. Heterogeneous Photocatalyst Materials for Water Splitting. *Chem. Soc. Rev.* **2009**, *38*, 253−278.

(24) Liao, J.; Sa, B.; Zhou, J.; Ahuja, R.; Sun, Z. Design of High-efficiency Visible-light Photocatalysts for Water Splitting: MoS2/AlN (GaN) Heterostructures. *J. Phys. Chem. C* **2014**, *118*, 17594−17599.
(25) Gong, Y.; Lin, J.; Wang, X.; Shi, G.; Lei, S.; Lin, Z.; Zou, X.; Ye, G.; Vajtai, R.; Yakobson, B.; et al. Vertical and In-plane Heterostructures from WS2/MoS2Monolayers. *Nat. Mater.* **2014**, *13*, 1135−1142.
(26) You, B.; Tang, M.; Tsai, C.; Abild Pedersen, F.; Zheng, X.; Li, H. Enhancing Electrocatalytic Water Splitting by Strain Engineering. *Adv. Mater.* **2019**, *31*, 1807001.
(27) He, Q.; Wu, Y.; Yang, C.; Zhang, H.; Tang, D.; Shang, X.; Wang, X. Switch Effect on Controlled Water Splitting by Biaxial Strain Regulating the Promising Two-dimensional Janus X2PAs (X = Si, Ge and Sn) Photocatalyst. *Nanoscale* **2023**, *15*, 10458−10464.
(28) Luo, Y.; Wang, S.; Shu, H.; Chou, J. P.; Ren, K.; Yu, J.; Sun, M. A MoSSe/Blue Phosphorene vdW Heterostructure with Energy Conversion Efficiency of 19.9% for Photocatalytic Water Splitting. *Semicond. Sci. Technol.* **2020**, *35*, 125008.
(29) Ren, K.; Wang, K.; Luo, Y.; Sun, M.; Altalhi, T.; Yakobson, B. I.; Zhang, G. Ultralow Frequency Interlayer Mode from Suppressed van der Waals Coupling in Polar Janus SMoSe/SWSe Heterostructure. *Mater. Today Phys.* **2025**, *53*, 101689.
(30) Zhang, C.; Ren, K.; Wang, S.; Luo, Y.; Tang, W.; Sun, M. Recent Progress on Two-dimensional van der Waals Heterostructures for Photocatalytic Water Splitting: A Selective Review. *J. Phys. D: Appl. Phys.* **2023**, *56*, 483001.
(31) Zhang, L.; Wu, B.; Li, Q.; Li, J. Molecular Engineering Lithium Sulfur Battery Cathode Based on Small Organic Molecules: An Ab-initio Investigation. *Appl. Surf. Sci.* **2019**, *484*, 1184−1190.
(32) Wang, S.; Tian, H.; Luo, Y.; Yu, J.; Ren, C.; Sun, C.; Xu, Y.; Sun, M. First-principles Calculations of Aluminium Nitride Monolayer with Chemical Functionalization. *Appl. Surf. Sci.* **2019**, *481*, 1549−1553.
(33) Yan, Y.; Chen, K.; Sun, M.; Ma, Y.; Wang, P.; Deng, J.; Zhang, X.; Liu, J. Z. Deciphering the Stability of Two-dimensional III-V Semiconductors: Building Blocks and Their Versatile Assembly. *Sci. Adv* **2025**, *11*, No. eadu5294.
(34) Tsipas, P.; Kassavetis, S.; Tsoutsou, D.; Xenogiannopoulou, E.; Golias, E. G. S. A.; Giamini, S. A.; Grazianetti, C.; Chiappe, D.; Molle, A.; Fanciulli, M.; et al. Evidence for Graphite-like Hexagonal AlN Nanosheets Epitaxially Grown on Single Crystal Ag (111). *Appl. Phys. Lett.* **2013**, *103*, 251605.
(35) Chang, S. J.; Wang, S. Y.; Huang, Y. C.; Chih, J. H.; Lai, Y. T.; Tsai, Y. W.; Lin, J. M.; Chien, C. H.; Tang, Y. T.; Hu, C. van der Waals epitaxy of 2D h -AlN on TMDs by atomic layer deposition at 250 °C. *Appl. Phys. Lett.* **2022**, *120*, 162102.
(36) Wang, S. Y.; Chang, S. J.; Huang, Y. C.; Chih, J. H.; Lin, Y. C.; Cheng, C. C.; Radu, I.; Hu, C.; Chien, C. H. Conformal Bilayer h-AlN Epitaxy on WS2 by ALD with Ultralow Leakage Current. *Appl. Phys. Lett.* **2023**, *123*, 162101.
(37) Idrees, M.; Nguyen, C. V.; Bui, H. D.; Ahmad, I.; Amin, B. Van der Waals Heterostructures Based on MSSe (M = Mo, W) and Graphene-like GaN: Enhanced Optoelectronic and Photocatalytic Properties for Water Splitting. *Phys. Chem. Chem. Phys.* **2020**, *22*, 20704−20711.
(38) Geim, A.; Grigorieva, I. van der Waals Heterostructures. *Nature* **2013**, *499*, 419−425.
(39) He, J.; Hummer, K.; Franchini, C. Stacking Effects on the Electronic and Optical Properties of Bilayer Transition Metal Dichalcogenides MoS2, MoSe2, WS2, and WSe2. *Phys. Rev. B* **2014**, *89*, 075409.
(40) Yin, W.; Wen, B.; Ge, Q.; Zou, D.; Xu, Y.; Liu, M.; Wei, X.; Chen, M.; Fan, X. Role of Intrinsic Dipole on Photocatalytic Water Splitting for Janus MoSSe/Nitrides Heterostructure: A First-principles Study. *Prog. Nat. Sci.: Mater. Int.* **2019**, *29*, 335−340.
(41) Giannozzi, P.; Baroni, S.; Bonini, N.; Calandra, M.; Car, R.; Cavazzoni, C.; Ceresoli, D.; Chiarotti, G.; Cococcioni, M.; Dabo, I.; et al. QUANTUM ESPRESSO: A Modular and Open-source Software Project for Quantum Simulations of Materials. *J. Phys.: condens. Matter* **2009**, *21*, 395502.
(42) Perdew, J.; Burke, K.; Ernzerhof, M. Generalized Gradient Approximation Made Simple. *Phys. Rev. Lett.* **1996**, *77*, 3865.
(43) Goedecker, S.; Teter, M.; Hutter, J. Separable Dual-space Gaussian Pseudopotentials. *Phys. Rev. B* **1996**, *54*, 1703.
(44) Hartwigsen, C.; Goedecker, S.; Hutter, J. Relativistic Separable Dual-space Gaussian Pseudopotentials from H to Rn. *Phys. Rev. B* **1998**, *58*, 3641.
(45) Monkhorst, H.; Pack, J. Special Points for Brillouin-zone Integrations. *Phys. Rev. B* **1976**, *13*, 5188.
(46) Grimme, S.; Antony, J.; Ehrlich, S.; Krieg, H. A consistent and accurate ab initio parametrization of density functional dispersion correction (DFT-D) for the 94 elements H-Pu. *J. Chem. Phys.* **2010**, *132*, 154104.
(47) Heyd, J.; Scuseria, G.; Ernzerhof, M. Hybrid Functionals Based on a Screened Coulomb Potential. *J. Chem. Phys.* **2003**, *118*, 8207−8215.
(48) Marzari, N.; Vanderbilt, D.; De Vita, A.; Payne, M. Thermal Contraction and Disordering of the Al (110) Surface. *Phys. Rev. Lett.* **1999**, *82*, 3296.
(49) Gonze, X.; Lee, C. Dynamical Matrices, Born Effective Charges, Dielectric Permittivity Tensors, and Interatomic Force Constants from Density-functional Perturbation Theory. *Phys. Rev. B* **1997**, *55*, 10355.
(50) Togo, A.; Tanaka, I. First Principles Phonon Calculations in Materials Science. *Scr. Mater.* **2015**, *108*, 1−5.
(51) Patouillard, J.; Bernard, M.; Cadot, S.; Gassilloud, R.; Bernier, N.; Grenier, A.; Mantoux, A.; Blanquet, E.; Martin, F.; Raynaud, C.; et al. MoS2-assisted Growth of Highly-oriented AlN Thin Films by Low-temperature van der Waals Epitaxy. *J. Vac. Sci. Technol., A* **2024**, *42*, 050401.
(52) Lee, C.; Wei, X.; Kysar, J.; Hone, J. Measurement of the Elastic Properties and Intrinsic Strength of Monolayer Graphene. *Science* **2008**, *321*, 385−388.
(53) Huang, M.; Yan, H.; Heinz, T. F.; Hone, J. Probing Strain-induced Electronic Structure Change in Graphene by Raman Spectroscopy. *Nano Lett.* **2010**, *10*, 4074−4079.
(54) Bertolazzi, S.; Brivio, J.; Kis, A. Stretching and Breaking of Ultrathin MoS2. *ACS Nano* **2011**, *5*, 9703−9709.
(55) Lakshmy, S.; Mondal, B.; Kalarikkal, N.; Rout, C. S.; Chakraborty, B. Recent Developments in Synthesis, Properties, and Applications of 2D Janus MoSSe and MoSexS(1-x) Alloys. *Adv. Powder Mater.* **2024**, *3*, 100204.
(56) Peng, Q.; Liang, C.; Ji, W.; De, S. Mechanical Properties of g-GaN: A First Principles Study. *Appl. Phys. A* **2013**, *113*, 483−490.
(57) Wang, G.; Dang, S.; Zhang, P.; Xiao, S.; Wang, C.; Zhong, M. Hybrid Density Functional Study on the Photocatalytic Properties of AlN/MoSe2, AlN/WS2, and AlN/WSe2 Heterostructures. *J. Phys. D: Appl. Phys.* **2018**, *51*, 025109.

https://doi.org/10.1021/acsaelm.5c01588
ACS Appl. Electron. Mater. 2025, 7, 10172−10185